

WACCN: Supplementary Notes

Jiayu Ellie Su *et al.*

Contents

1 Wavelet Transforms, Grid Resampling, and Anisotropy Metrics (S1)	2
1.1 Grid Resampling and Spot Alignment (S1.1)	2
1.2 Tissue Masking and Background Removal (S1.2)	2
1.3 DWT and DTCWT Implementation Details (S1.3)	3
1.4 Smoothing and Feature Alignment (S1.4)	3
1.5 Corridor Pooling and Orientation Estimation (S1.5)	3
1.6 Kernel Parameterization and Hyperparameters (S1.6)	4
1.7 Anisotropy Metrics and Coherence Length (S1.7)	4
1.8 Wavelet Filter Banks (S1.8)	5
2 CCC Inference, Null Models, and Pathways (S2)	5
2.1 Ligand/Receptor Preprocessing (S2.1)	5
2.2 Secreted vs Membrane-bound Ligands (S2.2)	5
2.3 Matched-marginal Null Model and FDR (S2.3)	5
2.4 Pathway Aggregation and Normalization (S2.4)	6
2.5 Additional CCC Visualizations (S2.5)	6
2.6 Benchmarking Details vs CellChat and COMMOT (S2.6)	7
2.7 ECM/Collagen Pathway Analyses (S2.7)	7
3 Graph Construction, Segmentation, and Autoencoder (S3)	7
3.1 DSAG Construction and Edge Weights (S3.1)	7
3.2 Macro-Regions and Zonal Compartments (S3.2)	8
3.3 Micro-Niches and Spatial Smoothing (S3.3)	8
3.4 Multi-view Autoencoder Objective (S3.4)	8
3.5 Consensus Structures (S3.5)	9
3.6 Evaluation Metrics and Implementation Details (S3.6)	9
4 Extended Results (S4)	10
4.1 Datasets (S4.1)	10
4.2 Histology-guided Anisotropy (S4.2)	10
4.3 Effects of Anisotropy on CCC Inference (S4.3)	12
4.4 Benchmarking vs Existing CCC Methods (S4.4)	15
4.5 Niche Identification and Consensus Structures (S4.5)	16
4.6 ECM/Collagen Case Study (S4.6)	18
4.7 Appendix: Cross-family Anisotropy Panels (S4.7)	18
4.8 ECM/Collagen Support Figures (S4.8)	19

Overview

These Supplementary Notes provide extended methods, derivations, and additional results for the WACCN framework described in the main manuscript. Section labels (e.g., S1.2, S3.4, S4.2) are referenced directly in the main text.

1 Wavelet Transforms, Grid Resampling, and Anisotropy Metrics (S1)

1.1 Grid Resampling and Spot Alignment (S1.1)

Visium spots are arranged on a hexagonal lattice. For wavelet analysis, we construct a square grid $X \in \mathbb{R}^{D \times D}$ as follows:

1. Compute the bounding box of the spot coordinates in the original image coordinate system.
2. Choose D so that the grid cell size is approximately one spot diameter; we use $D \in [128, 256]$ depending on field-of-view size.
3. For each grid cell, average the expression of all spots whose centers fall inside the cell. Cells with no spots are set to zero.
4. Store a mapping from each Visium spot to its nearest grid cell for later back-alignment of wavelet features.

All cellwise resampling affects only wavelet-based channels. CCC inference always uses spot-level expression at the original coordinates. We confirmed robustness to D by repeating analyses with $\pm 25\%$ grid resolution.

1.2 Tissue Masking and Background Removal (S1.2)

H&E images are first converted from RGB to HSV. We use a combination of hue and saturation thresholds to isolate tissue:

1. Compute global histograms of hue and saturation.
2. Identify dominant tissue peaks and choose loose thresholds around these peaks (typically $S > 0.1$ and hue excluding pure background ranges).
3. Apply thresholds to obtain a coarse tissue mask M_0 .
4. Perform color deconvolution with a standard hematoxylin/eosin matrix to refine M_0 by requiring sufficient hematoxylin intensity.
5. Apply morphological closing followed by small-hole filling to obtain a final binary mask M .

Mask-aware averaging for a scalar field X is implemented as

$$\bar{X}(\mathbf{p}) = \frac{\sum_{\mathbf{q}} K(\mathbf{p} - \mathbf{q}) M(\mathbf{q}) X(\mathbf{q})}{\sum_{\mathbf{q}} K(\mathbf{p} - \mathbf{q}) M(\mathbf{q}) + \varepsilon},$$

where K is a Gaussian kernel and ε is a small constant to avoid division by zero. Corridor pooling (S1.5) uses the same masked averaging formulation. Sensitivity analyses with one-pixel erosion/dilation of M showed that anisotropy estimates and CCC patterns are stable to modest mask perturbations.

1.3 DWT and DTCWT Implementation Details (S1.3)

For the real M -band DWT, we use compact orthogonal filters:

- $M = 2$: Daubechies 4-tap and 8-tap filters.
- $M = 3$ and $M = 4$: orthogonal filter banks from the literature with approximately uniform angular coverage.

Boundary handling is performed via symmetric extension. Subbands are re-expanded to the full grid size using nearest-neighbor upsampling and cropping, and then evaluated at spot coordinates by taking the value at the nearest pixel center.

For the 2D DTCWT, we use Kingsbury Q-shift filter sets with six oriented subbands per scale at nominal angles $15^\circ, 45^\circ, 75^\circ, 105^\circ, 135^\circ, 165^\circ$. For each subband b , we record both magnitude $|W_b|$ and a local phase-coherence measure κ_b , computed as the magnitude of the local complex mean over a small (5×5) window. Subbands with low κ_b contribute less to the orientation estimate via the weights ω_b .

1.4 Smoothing and Feature Alignment (S1.4)

Let Z_b denote a wavelet subband (either DWT or DTCWT). We smooth each subband with a Gaussian kernel with standard deviation equal to one spot radius in pixel units. The smoothed field \tilde{Z}_b is then sampled at spot centers using bilinear interpolation. These spot-level values compose the histology and gene-wavelet feature vectors used by the morphology gate and multi-view autoencoder.

We verified that doubling or halving the smoothing bandwidth produced qualitatively similar anisotropy patterns and CCC results, confirming that our findings are not tightly tuned to a specific bandwidth.

1.5 Corridor Pooling and Orientation Estimation (S1.5)

For a candidate directed edge $(i \rightarrow j)$ with displacement vector $\Delta\mathbf{x}_{ij}$, we define a local coordinate system where the s -axis is aligned with $\Delta\mathbf{x}_{ij}$ and the t -axis is orthogonal:

$$\Delta\mathbf{x}_{ij} = \begin{pmatrix} \Delta x \\ \Delta y \end{pmatrix}, \quad \hat{\mathbf{s}} = \frac{\Delta\mathbf{x}_{ij}}{\|\Delta\mathbf{x}_{ij}\|}, \quad \hat{\mathbf{t}} = \begin{pmatrix} -\hat{s}_y \\ \hat{s}_x \end{pmatrix}.$$

For each pixel location \mathbf{p} we compute

$$s(\mathbf{p}) = (\mathbf{p} - \mathbf{x}_i) \cdot \hat{\mathbf{s}}, \quad t(\mathbf{p}) = (\mathbf{p} - \mathbf{x}_i) \cdot \hat{\mathbf{t}}.$$

Corridor pooling for subband b is defined as

$$\bar{P}_b(i \rightarrow j) = \sum_{\mathbf{p}} \exp\left(-\frac{(s(\mathbf{p}) - s_{ij}/2)^2}{2\sigma_s^2}\right) \exp\left(-\frac{t(\mathbf{p})^2}{2\sigma_t^2}\right) M(\mathbf{p}) |Z_b(\mathbf{p})|,$$

where $s_{ij} = \|\Delta\mathbf{x}_{ij}\|$, σ_s controls spread along the edge, and σ_t controls the perpendicular corridor width. We typically take $\sigma_s \approx s_{ij}/2$ and σ_t equal to one to two spot diameters.

The doubled-angle resultant encodes orientation and anisotropy strength:

$$m(i \rightarrow j) = \sum_b \omega_b(i \rightarrow j) \bar{P}_b(i \rightarrow j) e^{2i\theta_b},$$

where θ_b is the nominal orientation of subband b and $\omega_b \propto \kappa_b$ (DTCWT) or a fixed reliability weight (DWT). The principal axis and normalized anisotropy strength are

$$\theta_{ij}^* = \frac{1}{2} \arg m(i \rightarrow j), \quad r_{ij} = \frac{|m(i \rightarrow j)|}{\sum_b \omega_b \bar{P}_b(i \rightarrow j) + \varepsilon}.$$

1.6 Kernel Parameterization and Hyperparameters (S1.6)

We map r_{ij} to an axis ratio

$$a_{ij} = 1 + (a_{\max} - 1)r_{ij}^\gamma,$$

with $a_{\max} \in [2.5, 3]$ and $\gamma \in [1, 2]$; we use $a_{\max} = 3, \gamma = 1.5$ in the main experiments. The elliptical Gaussian kernel in (s, t) coordinates is

$$\tilde{K}_{i \rightarrow j} = \exp\left(-\frac{\Delta s_{ij}^2}{2\sigma_{\parallel}^2} - \frac{\Delta t_{ij}^2}{2\sigma_{\perp}^2}\right),$$

with $\sigma_{\parallel} = \sigma_0 a_{ij}$ and $\sigma_{\perp} = \sigma_0 / a_{ij}$, and σ_0 tied to the median nearest-neighbor distance h . We enforce $\sigma_{\perp} \geq \sigma_{\min}$ (one to two pixels) to avoid degenerate kernels.

The spatial radius $R = ah$ for candidate edges uses $\alpha \in [3, 5]$; we use $\alpha = 4$ in the main results.

1.7 Anisotropy Metrics and Coherence Length (S1.7)

For each spot i , we define an outgoing communication vector

$$\mathbf{v}_i = \sum_j w_{ij} \hat{\mathbf{u}}_{ij},$$

where $\hat{\mathbf{u}}_{ij}$ is the unit vector from i to j and w_{ij} is a weight (e.g., aggregated CCC strength). The angular concentration R_w is the mean resultant length:

$$R_w = \frac{1}{N} \sum_{i=1}^N \frac{\|\mathbf{v}_i\|}{\sum_j w_{ij} + \varepsilon}.$$

Global axial alignment is assessed by projecting all \mathbf{v}_i onto the best axis $\hat{\mathbf{n}}$ (found via PCA on direction vectors) and computing the mean squared projection; values near zero indicate no global preferred direction.

Neighborhood alignment compares \mathbf{v}_i to its neighbors:

$$A_{\text{neigh}} = \frac{1}{|\mathcal{E}|} \sum_{(i,j) \in \mathcal{E}} \frac{\mathbf{v}_i \cdot \mathbf{v}_j}{\|\mathbf{v}_i\| \|\mathbf{v}_j\| + \varepsilon}.$$

For the orientation variogram, we convert orientations $\theta(\mathbf{x}) \in [0, \pi)$ to unit axial vectors $\mathbf{q}(\mathbf{x}) = (\cos 2\theta(\mathbf{x}), \sin 2\theta(\mathbf{x}))$ and compute

$$\gamma(h) = \frac{1}{2|\mathcal{P}(h)|} \sum_{(\mathbf{x}, \mathbf{y}) \in \mathcal{P}(h)} \|\mathbf{q}(\mathbf{x}) - \mathbf{q}(\mathbf{y})\|_2^2,$$

where $\mathcal{P}(h)$ is the set of point pairs separated by distance h within a small tolerance. The coherence length L_c is defined as the smallest h at which $\gamma(h)$ reaches 95% of its plateau.

1.8 Wavelet Filter Banks (S1.8)

For reproducibility, we summarize the wavelet families used in the main experiments:

- **2-band families (wv22/23/24):** separable real DWTs using compact orthogonal Daubechies-like filters (4-tap and 8-tap variants) with standard horizontal/vertical/diagonal orientations.
- **4-band families (wv42/44):** real $M=4$ -band filter banks with approximately uniform angular coverage over $[0, \pi]$, producing multiple oriented detail subbands per scale (e.g., near $0^\circ, 45^\circ, 90^\circ, 135^\circ$).
- **DTCWT:** dual-tree complex wavelet transform with Q-shift filters and six approximately analytic oriented subbands per scale at nominal angles $15^\circ, 45^\circ, 75^\circ, 105^\circ, 135^\circ, 165^\circ$.

Exact filter taps, orientation lookup tables, and configuration files for wv22/23/24, wv42/44, and DTCWT are provided in the public repository (<https://github.com/esu28/WACCCN>) under the `filters/` directory.

2 CCC Inference, Null Models, and Pathways (S2)

2.1 Ligand/Receptor Preprocessing (S2.1)

Raw counts are library-size normalized and log-transformed using standard Seurat/Scanpy workflows. For CCC, we winsorize expression at the 99th percentile per gene and rescale to $[0, 1]$:

$$\hat{E}_{i,g} = \frac{\min(E_{i,g}, q_{0.99}(g)) - \min_k E_{k,g}}{\max_k \min(E_{k,g}, q_{0.99}(g)) - \min_k E_{k,g} + \varepsilon}.$$

Genes with very low detection across spots are excluded from CCC analysis.

2.2 Secreted vs Membrane-bound Ligands (S2.2)

We distinguish secreted and membrane-bound ligands using curated annotations. For secreted ligands, the kernel

$$\tilde{K}_{i \rightarrow j}^{\text{sec}} = K_{i \rightarrow j}^{\text{eff}} \exp(-(d_{ij}/W_r)^2),$$

uses $W_r = \lambda \bar{d}_{k\text{-NN}}$ with $\lambda \in [1.5, 3]$ and $k = 5$. For membrane-bound ligands, we set

$$\tilde{K}_{i \rightarrow j}^{\text{mb}} = \mathbb{I}\{d_{ij} \leq R_{\text{contact}}\} K_{i \rightarrow j}^{\text{eff}},$$

with R_{contact} typically one to two spot spacings.

The ligand contribution is $C_{i \rightarrow j}(L) = \hat{E}_{i,L} \tilde{K}_{i \rightarrow j}^{\bullet}$, where \bullet is either “sec” or “mb”.

2.3 Matched-marginal Null Model and FDR (S2.3)

To control for marginal expression patterns, we construct null ligand and receptor genes with similar marginal distributions:

1. For each ligand L , compute its global mean expression and assign it to a bin based on quantiles (e.g., deciles).
2. For each receptor R , perform the same binning.

3. For each true pair (L, R) , generate n_{null} null pairs (L', R') by drawing L' uniformly from ligands in the same bin as L and R' from receptors in the same bin as R , with replacement.
4. For each (L', R') , compute CCC scores $\tilde{H}_{i \rightarrow j}(L', R')$ using the same kernels K^{eff} and morphology gate $G_{i \rightarrow j}$.

For each edge $(i \rightarrow j)$ and true pair (L, R) , we obtain an empirical p -value as

$$p_{ij}^{(L,R)} = \frac{1 + \#\{\tilde{H}_{i \rightarrow j}(L', R') \geq \tilde{H}_{i \rightarrow j}(L, R)\}}{1 + n_{\text{null}}}.$$

We then apply Benjamini–Hochberg FDR control across all edges and pairs per dataset, and zero out non-significant edges.

In the main experiments, we use $n_{\text{null}} = 200$ and an FDR threshold of $q = 0.05$. We verified that using $n_{\text{null}} = 100$ yields similar rankings of significant edges at reduced computational cost.

2.4 Pathway Aggregation and Normalization (S2.4)

Let $S_{i \rightarrow j}^{L,R}$ denote the final CCC score for pair (L, R) (e.g., $\tilde{H}_{i \rightarrow j}(L, R)$ after TF modulation and significance filtering). For a pathway P defined as a set of ligand–receptor pairs, we define

$$S_{i \rightarrow j}^P = \frac{1}{|P|} \sum_{(L,R) \in P} S_{i \rightarrow j}^{L,R}.$$

To avoid domination by a few extremely strong edges, we optionally perform a row-wise soft normalization:

$$\tilde{S}_{i \rightarrow j}^P = \frac{S_{i \rightarrow j}^P}{\sum_k S_{i \rightarrow k}^P + \varepsilon},$$

yielding a quasi-probabilistic distribution of outgoing mass for each sender and pathway. For embedding and clustering, we use either $S_{i \rightarrow j}^P$ or $\log(1 + \tilde{S}_{i \rightarrow j}^P)$ depending on dynamic range.

2.5 Additional CCC Visualizations (S2.5)

To diagnose CCC patterns, we use:

- Edge-length distributions for isotropic vs anisotropic kernels.
- Histograms of edge angles and local angular concentration R_w .
- Vector-field overlays of dominant outgoing CCC direction per spot.
- Sender- and receiver-strength maps per pathway and Macro-Region.

These visualizations confirm that anisotropy concentrates CCC along stromal bands and suppresses implausible long-range edges.

2.6 Benchmarking Details vs CellChat and COMMOT (S2.6)

For CellChat v2 and COMMOT, we use recommended parameters for Visium data and the same ligand–receptor databases where possible. To compare methods, we compute:

- The number of significant ligand–receptor pairs.
- Pairwise overlaps between prediction sets.
- Edge-level false-positive rates estimated using our matched-marginal nulls (applied to each method’s predictions).

Spatial coherence is quantified by the mean neighborhood alignment A_{neigh} (Section S1.7) and by a local edge-density measure within stromal vs tumor–epithelium Macro-Regions.

2.7 ECM/Collagen Pathway Analyses (S2.7)

For ECM/Collagen, we focus on a curated subset of collagen- and ECM-related ligand–receptor pairs. We summarize:

- Stromal vs epithelial sending and receiving strength.
- Sender-overlap matrices across stromal clusters.
- Edge-length distributions restricted to ECM/Collagen.
- Bipartite ribbon plots highlighting dominant stromal→epithelial flows.

Stromal clusters with high ECM/Collagen outflow show sharp spatial confinement to bands adjacent to tumor epithelium, consistent with invasion-associated ECM remodeling.

3 Graph Construction, Segmentation, and Autoencoder (S3)

3.1 DSAG Construction and Edge Weights (S3.1)

We build a directed spatial adjacency graph (DSAG) using radius- R neighborhoods:

1. For each spot i , find all spots j with $d_{ij} \leq R$, where $R = \alpha h$ and h is the median nearest-neighbor distance.
2. Assign an edge $(i \rightarrow j)$ with weight w_{ij} equal to a chosen CCC-based quantity, typically pathway-aggregated outflow $w_{ij} = \sum_P S_{i \rightarrow j}^P$.
3. Optionally construct a symmetrized adjacency for graph-based regularization: $w_{ij}^{\text{sym}} = w_{ij} + w_{ji}$.

The DSAG is used both for evaluating anisotropy (via edge directions) and as one of the inputs to the multi-view autoencoder (through a Laplacian-based smoothness term).

3.2 Macro-Regions and Zonal Compartments (S3.2)

Macro-Regions. We tile the H&E image into non-overlapping $T \times T$ patches, typically $T = 256$ px, and train a U-Net with encoder initialized from ImageNet-pretrained weights. When ground-truth labels are available (e.g., tumor, stroma, background), we use cross-entropy loss with mild class reweighting. Inference produces a probability map per class; we assign each pixel to the class with maximum probability and then project to spots via majority vote within each spot’s footprint.

Zonal Compartments. Within each Macro-Region, we compute the distance transform to the nearest boundary between distinct Macro-Regions. Spots are categorized into:

- *Core*: distance above a high threshold (deep interior).
- *Edge*: distance below a low threshold but still inside the Macro-Region.
- *Transitory/mixed*: intermediate distances or regions with high local label entropy (mixed neighborhoods).

We smooth zone labels using one or two rounds of majority voting over geodesic k -nearest neighbors. Thresholds are chosen as fractions of the Macro-Region’s characteristic size and are robust over a broad range.

3.3 Micro-Niches and Spatial Smoothing (S3.3)

Within each (Macro-Region, Zonal Compartment) combination, we define a feature matrix $F \in \mathbb{R}^{N_{\text{sub}} \times d_{\text{feat}}}$ combining log-normalized expression for selected marker genes and smoothed histology wavelet channels. We optionally append TF scores.

We apply dimensionality reduction (PCA) followed by clustering (e.g., Leiden or K-means) to define Micro-Niches. To avoid spurious single-spot clusters, we apply a label smoothing step:

1. For each spot, examine a fixed number ($k = 8\text{--}12$) of nearest neighbors.
2. If the spot’s label disagrees with the majority by a large margin, reassign it to the majority label.

This yields Micro-Niches that are contiguous and morphologically interpretable without blurring across Macro-Region boundaries.

3.4 Multi-view Autoencoder Objective (S3.4)

For each view v (genes, TFs, histology wavelets, gene-wavelets, hierarchical labels, CCC features), we define an encoder $f_v : \mathbb{R}^{d_v} \rightarrow \mathbb{R}^{d_{\text{latent}}}$ with two hidden layers (64 and 32 units, ReLU activations). View-specific embeddings are concatenated and projected to a shared latent representation $Z \in \mathbb{R}^{N \times d}$.

The total loss is

$$\mathcal{L} = \mathcal{L}_{\text{recon}} + \lambda_{\text{Lapl}} \mathcal{L}_{\text{Lapl}} + \lambda_{\text{InfoNCE}} \mathcal{L}_{\text{InfoNCE}} + \lambda_{\text{DEC}} \mathcal{L}_{\text{DEC}}.$$

Reconstruction loss. Each view has a decoder \tilde{f}_v with symmetric architecture. We use mean-squared error for continuous views (genes, wavelets, CCC) and cross-entropy for one-hot label views:

$$\mathcal{L}_{\text{recon}} = \sum_v \alpha_v \ell_v(X^{(v)}, \tilde{f}_v(Z)),$$

with weights α_v chosen so that each view contributes on a similar scale.

CCC-Laplacian loss. Let W be a row-stochastic CCC affinity constructed as a simplex-weighted combination of pathway matrices. The normalized graph Laplacian is $L = I - \frac{1}{2}(W + W^\top)$. We define

$$\mathcal{L}_{\text{Lapl}} = \frac{1}{N} \text{Tr}(Z^\top L Z),$$

encouraging nearby nodes in the CCC graph to have similar embeddings.

Contrastive InfoNCE loss. We construct two augmented views of Z via small Gaussian noise and dropout. We then apply an InfoNCE loss with temperature τ to bring augmentations of the same spot closer while pushing different spots apart.

Deep embedded clustering (DEC) loss. We initialize cluster centers in latent space via K-means and use a soft assignment Q (Student-t kernel) and target distribution P as in DEC. The clustering loss is the Kullback–Leibler divergence $\mathcal{L}_{\text{DEC}} = \text{KL}(P\|Q)$, periodically updating cluster centers and P .

3.5 Consensus Structures (S3.5)

Clusters obtained from the latent space define candidate Consensus Structures. We optionally:

1. Restrict clusters to be homogeneous with respect to Macro-Region by splitting clusters that span multiple Macro-Regions.
2. Apply one additional round of spatial label smoothing (as in Micro-Niches) using a graph based on Euclidean distance or DSAG adjacency.
3. Merge tiny clusters (below a small fraction of spots) into the most similar neighboring cluster in latent space.

The resulting set of cluster labels constitutes the final Consensus Structures reported in the main text.

3.6 Evaluation Metrics and Implementation Details (S3.6)

We evaluate partition quality against pathologist-provided labels using:

Adjusted Rand Index (ARI). For partitions U and V over N samples, ARI is

$$\text{ARI} = \frac{\sum_{ij} \binom{n_{ij}}{2} - [\sum_i \binom{a_i}{2} \sum_j \binom{b_j}{2}] / \binom{N}{2}}{\frac{1}{2} [\sum_i \binom{a_i}{2} + \sum_j \binom{b_j}{2}] - [\sum_i \binom{a_i}{2} \sum_j \binom{b_j}{2}] / \binom{N}{2}},$$

where n_{ij} is the number of samples in both cluster i of U and cluster j of V , $a_i = \sum_j n_{ij}$, and $b_j = \sum_i n_{ij}$.

Normalized mutual information (NMI). We compute NMI using the standard symmetric definition based on the mutual information and entropies of U and V .

V-measure, purity, F1, silhouette. We use conventional definitions as implemented in scikit-learn: V-measure as the harmonic mean of homogeneity and completeness, purity as the average cluster-wise majority fraction, macro/weighted F1 across labels, and silhouette using Euclidean distance in latent space.

Cluster labels are matched to pathologist annotations via the Hungarian algorithm before reporting class-wise metrics.

Code to reproduce all analyses, including configuration files for the main experiments and ablations, is available at:

<https://github.com/esu28/WACCN>

4 Extended Results (S4)

4.1 Datasets (S4.1)

We evaluated WACCN on two publicly available spatial transcriptomics datasets, each profiled using the 10x Genomics Visium platform: an oral squamous cell carcinoma (OSCC) sample and a human breast cancer (BRCA) slide. The OSCC slide contained $S=1185$ barcodes, while the BRCA slide contained $S=3547$ barcodes. OSCC exhibits relatively organized stromal architecture, whereas BRCA presents a more heterogeneous and fragmented tissue structure. These contrasting morphologies provide a natural test bed for assessing whether wavelet-derived anisotropy features generalize across tissues with different levels of organization.

4.2 Histology-guided Anisotropy (S4.2)

We first quantified histology-guided anisotropy on the OSCC slide ($S=1185$; median 1-NN scale $h=25$ px) and visualized the axial field inferred from H&E (Fig. 1).

Kernel elongation is widespread. The axis-ratio distribution $\rho = \sigma_{\parallel}/\sigma_{\perp}$ was consistently right-shifted (Fig. 1c). With DTCWT on OSCC, the median elongation was $\tilde{\rho}=1.627$ (equivalently $\tilde{a}=0.239$ with $a = (\rho-1)/(\rho+1)$), confirming that elongated kernels are the norm rather than the exception.

Functional consequence: anisotropy focuses outgoing mass. For each spot i , the outgoing angular concentration R_w (defined in Section S1.7) increased from $\tilde{R}_w^{\text{ISO}}=0.028$ to $\tilde{R}_w^{\text{ANISO}}=0.207$ under DTCWT, a nearly 7.4-fold gain (median $\Delta\tilde{R}_w=0.135$, bootstrap 95% CI [0.122, 0.143]; Wilcoxon one-sided $p=3.27\times 10^{-165}$; Fig. 1d). Thus, anisotropy produces sharper and more directional communication outflows.

Finite spatial coherence of orientations. The orientation variogram $\gamma(\delta)$ (Section S1.7) decayed toward a rotation-null envelope, with coherence length $L_c=400.5$ px ($\approx 16.0 h$), measured at the first crossing of 0.2 (Fig. 1e). This indicates that preferred orientations persist mesoscopically over hundreds of microns.

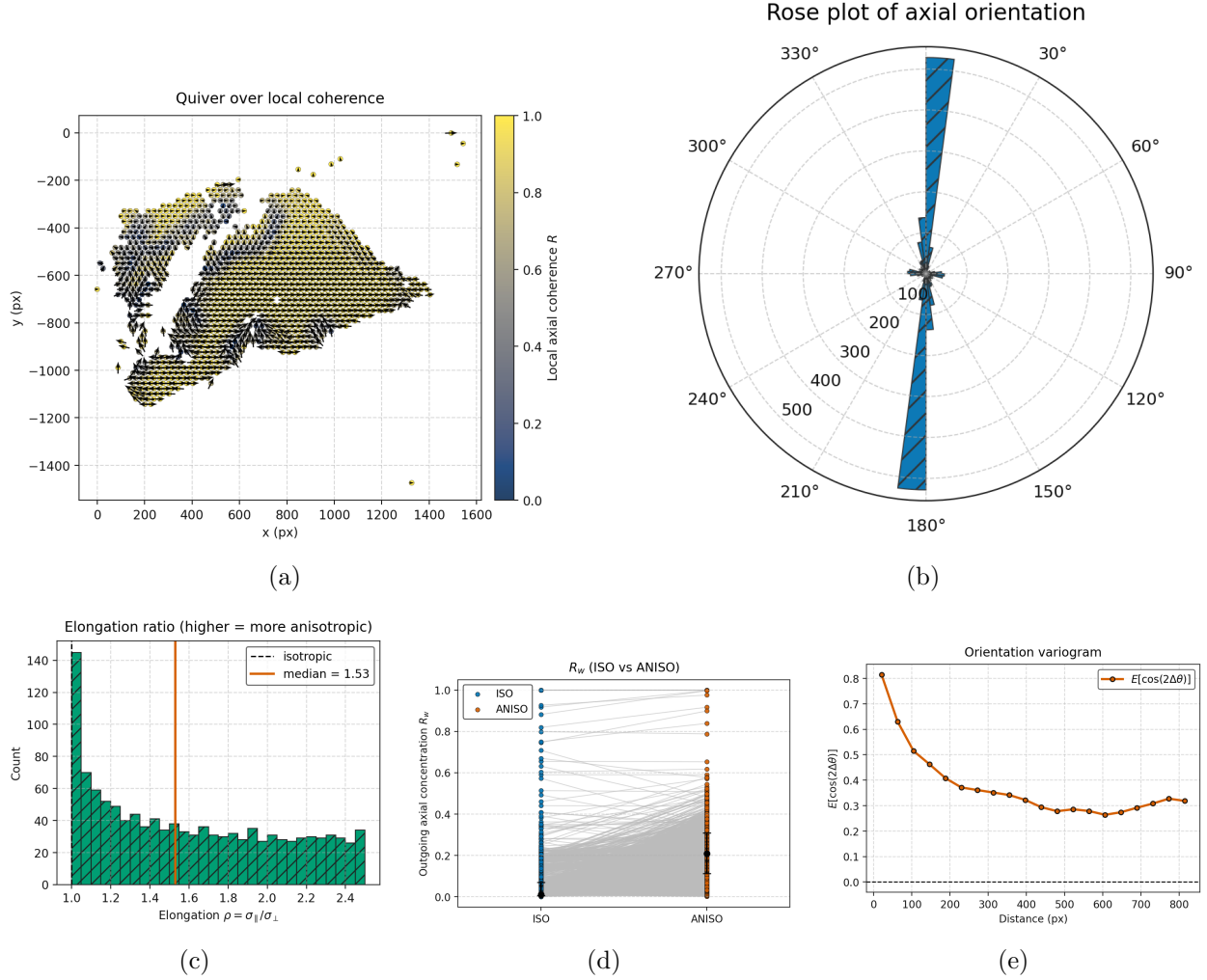


Figure 1: **Histology-guided anisotropy (DTCWT; OSCC).** (a) Quiver of dominant axis θ (arrow length $\propto a$) over local axial coherence R (dot color; radius $2h=50$ px). (b) Rose of axial orientations ($\theta \equiv \theta + \pi$). (c) Kernel elongation ρ (median $\tilde{\rho}=1.627$). (d) R_w shift from ISO to ANISO ($\Delta\tilde{R}_w=0.135$). (e) Orientation variogram; $L_c=400.5$ px ($\approx 16.0 h$).

Cross-method consistency. Across two-band, four-band, and DTCWT families, $\Delta\tilde{R}_w$ remained large and highly significant on OSCC (Table 1; see Supplementary Figs. S8–S10 for full OSCC family-level panels). Axial orientations agreed almost perfectly among two-band families (by construction), but agreement was reduced when compared with steered four-band or DTCWT families, which capture distinct orientation subspaces.

Controls. Baselines used area-matched isotropic kernels. Outgoing weights were normalized per sender, and variogram nulls were generated by random global rotations (and within-patch permutations when indicated).

Table 1: Cross-method anisotropy summary on OSCC. $S=1185$; median $h=25$ px.

Method	$\tilde{\rho}$	\tilde{a}	\tilde{R}_w^{ISO}	$\tilde{R}_w^{\text{ANISO}}$	$\Delta\tilde{R}_w$ [95% CI]	Wilcoxon p	L_c (px / h)	Axial agree vs wv22
wv22	1.531	0.210	0.028	0.212	0.141 [0.129, 0.154]	5.62×10^{-172}	NA	1.000
wv23	1.531	0.210	0.028	0.214	0.142 [0.129, 0.154]	1.43×10^{-172}	NA	0.878
wv24	1.531	0.210	0.028	0.215	0.145 [0.133, 0.155]	1.84×10^{-175}	NA	0.846
wv42	1.531	0.210	0.028	0.215	0.145 [0.130, 0.156]	9.97×10^{-171}	201.4 / 8.1	0.367
wv44	1.628	0.239	0.028	0.222	0.143 [0.132, 0.155]	1.38×10^{-173}	161.5 / 6.5	0.222
DTCWT	1.627	0.239	0.028	0.207	0.135 [0.122, 0.143]	3.27×10^{-165}	400.5 / 16.0	0.487

Replication on BRCA. On BRCA ($S=3547$; median $h=22$ px), all anisotropic families again yielded highly significant increases in R_w relative to isotropic baselines (Table 2; Supplementary Figs. S11–S13). Median $\Delta\tilde{R}_w$ ranged from 0.131 (wv24) to 0.172 (DTCWT), with Wilcoxon one-sided $p < 10^{-300}$ for all families. Unlike OSCC, however, the 2-band families (wv22/23/24) produced strong alignment gains but their variograms never crossed the 0.2 threshold, yielding undefined coherence lengths. The 4-band and DTCWT families delivered both alignment gains and finite coherence: wv44 achieved $\tilde{R}_w = 0.183$ with $L_c \approx 65$ px, while DTCWT reached $\tilde{R}_w = 0.212$ with $L_c \approx 63$ px.

Compared to OSCC, BRCA coherence scales were substantially shorter ($L_c \sim 63$ px $\approx 3h$ vs. $L_c \sim 400$ px $\approx 16h$). Biologically, this reflects the more heterogeneous and disorganized stromal environment in breast cancer, where preferred orientations decorrelate quickly and anisotropy cannot propagate over long distances. In contrast, OSCC exhibits more continuous stromal bands, supporting long-range coherence.

Table 2: Cross-method anisotropy summary on BRCA. $S=3547$; median $h=22$ px.

Method	$\tilde{\rho}$	\tilde{a}	\tilde{R}_w^{ISO}	$\tilde{R}_w^{\text{ANISO}}$	$\Delta\tilde{R}_w$ [95% CI]	Wilcoxon p	L_c (px)	Axial agree vs wv22
wv22	1.53	0.21	0.013	0.213	0.151 [0.145, 0.159]	$< 10^{-300}$	NA	1.000
wv23	1.53	0.21	0.013	0.213	0.151 [0.145, 0.159]	$< 10^{-300}$	NA	0.989
wv24	1.53	0.21	0.014	0.196	0.131 [0.124, 0.139]	$< 10^{-300}$	NA	0.976
wv42	1.53	0.21	0.014	0.181	0.139 [0.136, 0.142]	$< 10^{-300}$	47	0.062
wv44	1.53	0.21	0.014	0.183	0.139 [0.136, 0.143]	$< 10^{-300}$	65	0.286
DTCWT	1.53	0.21	0.013	0.212	0.172 [0.169, 0.177]	$< 10^{-300}$	63	0.035

Model family choice for downstream analyses. On OSCC, wv44 achieved the strongest local alignment ($\tilde{R}_w^{\text{ANISO}} = 0.222$) with finite coherence ($L_c \approx 161$ px), whereas DTCWT produced slightly weaker sharpening ($\tilde{R}_w = 0.207$) but the longest coherence ($L_c \approx 401$ px). wv42 fell in between. On BRCA, by contrast, DTCWT slightly outperformed wv44 in both alignment ($\tilde{R}_w = 0.212$ vs. 0.183) and coherence ($L_c = 63$ vs. 65 px).

Together, these results indicate complementary strengths: wv44 emphasizes sharper local anisotropy, while DTCWT captures broader-scale coherence and remains robust in more heterogeneous tissue. Accordingly, we adopt wv44 as our *default* family for CCC visualization and clustering, while using DTCWT in main anisotropy figures for its smoothness and cross-dataset consistency (see Section S4.7, Figs. S8–S13).

4.3 Effects of Anisotropy on CCC Inference (S4.3)

Global alignment (OSCC). On the OSCC slide ($S=1185$), whole-slide axial alignment A was near zero for both anisotropic (ANISO) and isotropic (ISO) CCC, with overlapping confidence

intervals (Table 3). This indicates that slide-level averaging cancels opposing domains and serves primarily as a global control, confirming that anisotropy does not introduce spurious whole-slide biases.

Table 3: Whole-slide CCC alignment metrics on OSCC ($S=1185$). A : global axial alignment; A_{rot90} : 90° control; \widetilde{AI} : median along-across index. CIs are bootstrap 95%.

Model	A [95% CI]	A_{rot90}	\widetilde{AI} [95% CI]
ISO	0.002 [-0.036, 0.039]	-0.002	0.158 [0.123, 0.190]
ANISO	-0.001 [-0.040, 0.037]	+0.001	0.153 [0.116, 0.184]

Neighborhood alignment (OSCC). At mesoscopic scales ($r = 40 \text{ px} \approx 1.6h$), anisotropy revealed clearer effects. Median neighborhood alignment $\widetilde{A}_{\text{neigh}}$ (Section S1.7) was unchanged, but directional coherence increased from $\widetilde{R}_{\text{neigh}} = 0.322$ (ISO) to 0.332 (ANISO) (Table 4). Difference maps highlighted tumor-stroma interfaces, where anisotropy reinforced along-axis preference by $\sim 0.03\text{--}0.05$. Thus, anisotropy sharpens CCC bundles precisely at morphological boundaries, where communication is most directional.

Table 4: Neighborhood-level CCC alignment metrics on OSCC ($r = 40 \text{ px}$). A_{neigh} : local axial alignment; R_{neigh} : neighborhood resultant magnitude.

Model	$\widetilde{A}_{\text{neigh}}$ [IQR]	$\widetilde{R}_{\text{neigh}}$	Notes
ISO	0.046 [-0.20, 0.20]	0.322	Baseline
ANISO	0.045 [-0.21, 0.19]	0.332	Sharper bundles; $\Delta R \approx +0.010$

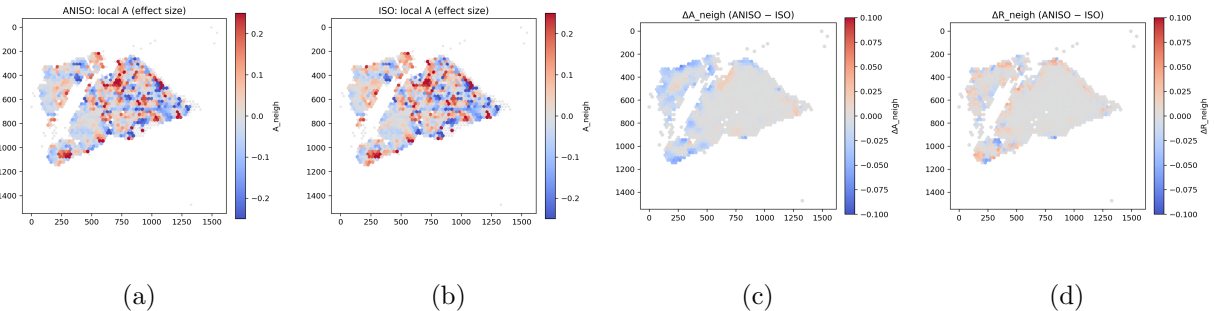


Figure 2: Neighborhood-level CCC alignment (OSCC, $r = 40 \text{ px}$). (a) ANISO A_{neigh} ; (b) ISO A_{neigh} ; (c) ΔA map; (d) ΔR map. Anisotropy strengthens directional coherence and highlights tumor-stroma boundaries with enhanced along-axis flow.

Direction of flow (OSCC). Vector fields of net CCC direction and coherence further illustrate these local differences. Under ANISO, communication vectors organized into continuous bundles that trace histological structures such as stromal bands and tumor boundaries. In contrast, ISO produced diffuse and scattered vectors (Fig. 3). This indicates that anisotropy amplifies spatial organization of CCC, converting noisy local interactions into coherent tissue-scale flows.

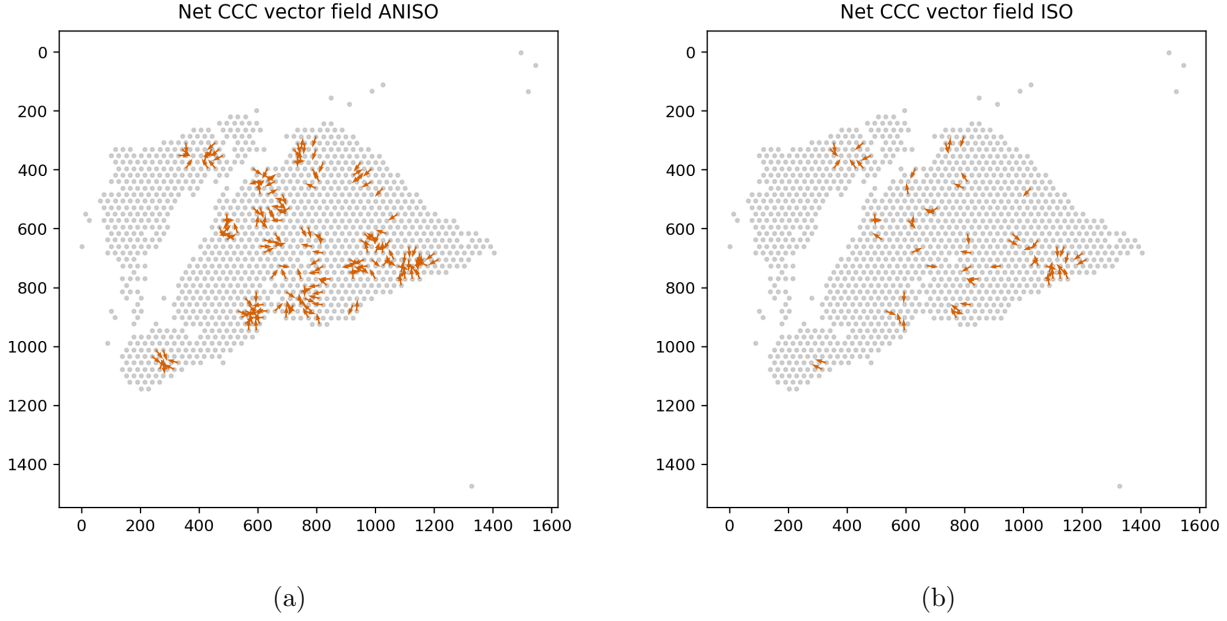


Figure 3: **Local CCC vector fields on OSCC.** (a) ANISO: net CCC vectors form coherent bundles aligned with histology. (b) ISO: vectors are diffuse and disorganized.

Replication on BRCA. On the BRCA slide ($S=3547$), anisotropy again did not introduce a global bias (Table 5). Median along-across indices \widetilde{AI} collapsed at zero, consistent with the much shorter anisotropy coherence length in BRCA (Table 2).

Table 5: Whole-slide CCC alignment metrics on BRCA ($S=3547$; DTCWT).

Model	A [95% CI]	A_{rot90}	\widetilde{AI} [95% CI]
ISO	-0.002 [-0.017, 0.012]	+0.002	0.000 [0, 0]
ANISO	+0.002 [-0.012, 0.017]	-0.002	0.000 [0, 0]

Neighborhood alignment (BRCA). Local analysis revealed only subtle effects: median $\widetilde{A}_{\text{neigh}}$ remained at zero, while $\widetilde{R}_{\text{neigh}}$ rose modestly under ANISO (0.301 vs. 0.296; Table 6). These small shifts are consistent with BRCA’s short coherence length ($L_c \approx 63$ px, $\sim 3h$). With orientations decorrelating after only a few spot spacings, anisotropy cannot propagate stable alignment across neighborhoods.

Table 6: Neighborhood-level CCC alignment metrics on BRCA ($r = 40$ px). Values reflect BRCA’s short coherence length ($L_c \approx 63$ px).

Model	$\widetilde{A}_{\text{neigh}}$ [IQR]	$\widetilde{R}_{\text{neigh}}$	Notes
ISO	0.000 [-0.19, 0.19]	0.296	Baseline
ANISO	0.001 [-0.20, 0.18]	0.301	Slight coherence gain; negligible A shift

Direction of flow (BRCA). Vector fields were broadly similar under ANISO and ISO (Fig. 4), both appearing diffuse and disorganized. Unlike OSCC, where long-range coherence ($L_c \approx 400$ px) supports contiguous bundles, the short coherence in BRCA ($L_c \approx 63$ px) causes orientations to decorrelate within ~ 3 spot spacings. Biologically, this reflects the fragmented and heterogeneous BRCA stroma: anisotropy exists locally, but does not propagate into coherent CCC flows across the tissue.

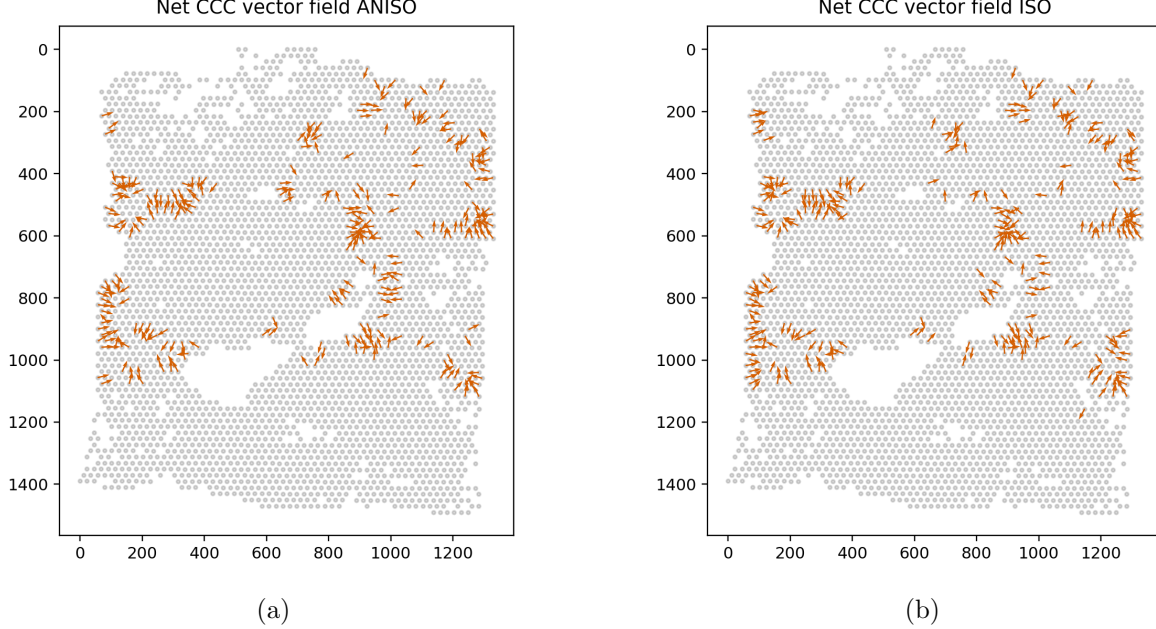


Figure 4: **Local CCC vector fields on BRCA.** (a) ANISO; (b) ISO. The short coherence length ($L_c \approx 63$ px, $\sim 3h$) causes orientations to decorrelate quickly, preventing anisotropy from producing stable bundles.

4.4 Benchmarking vs Existing CCC Methods (S4.4)

We benchmarked our framework against CellChat v2 and COMMOT on the BRCA dataset, using a 5% overlap threshold to define “unreliable” ligand–receptor pairs (LRPs).

Error rates. False positive rates (FPR) were lowest for our method (1.283%), compared to CellChat (3.848%) and COMMOT (6.452%) (Table 7). In addition, pairwise agreements were modest: CellChat and WACCCN shared $\sim 74\%$ of predictions, COMMOT overlapped less ($\sim 46\%$), and the two external methods agreed with each other at $\sim 68\%$.

Table 7: Benchmarking of CCC inference methods on BRCA. FPR = false positive rate; “Agreement” = fraction of method A’s predictions recovered by method B.

Method	FPR (%)	Agreement with Ours (%)	Agreement with Each Other (%)
Ours	1.283	—	—
CellChat	3.848	74.219	67.535
COMMOT	6.452	46.094	67.535

Interpretation. The relatively low FPR of our method reflects its geometry- and morphology-aware design, which penalizes spatially implausible edges. The modest overlaps between all methods—including between CellChat and COMMOT themselves—highlight the lack of a gold standard for CCC in spatial transcriptomics. Instead of direct accuracy, benchmarking should be read as a plausibility check: WACCCN consistently prioritizes morphologically coherent and locally constrained signaling, a feature particularly relevant in disorganized tissues such as BRCA where traditional approaches generate many diffuse or noisy edges.

4.5 Niche Identification and Consensus Structures (S4.5)

We examined niche structure from two complementary perspectives: (*i*) segmentation-driven maps (Macro-Regions, Zonal Compartments, Micro-Niches; default wv44; Section S3.2–S3.3) and (*ii*) clustering quality from the final autoencoder representation built on anisotropy-aware CCC (Section S3.4–S3.5). The first provides direct morphological context, while the second quantifies separability of functional niches without assuming one-to-one correspondence to pathologist labels.

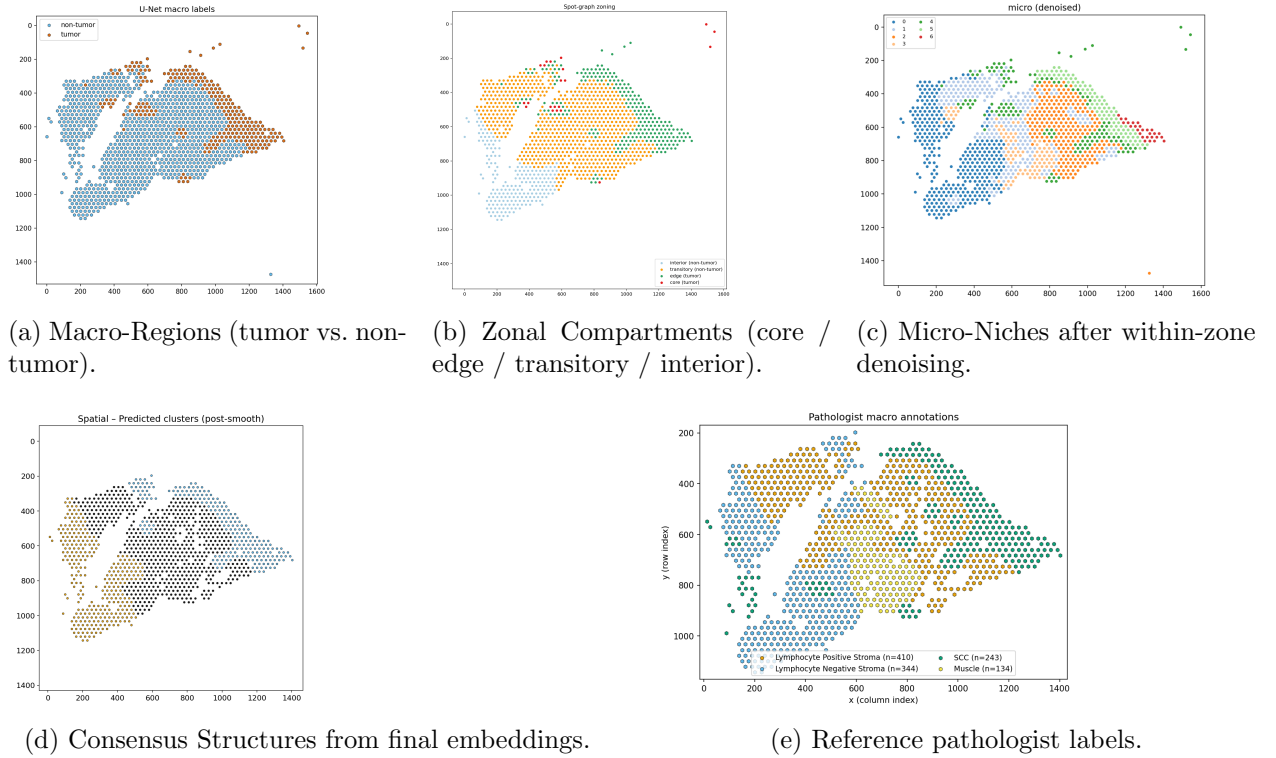
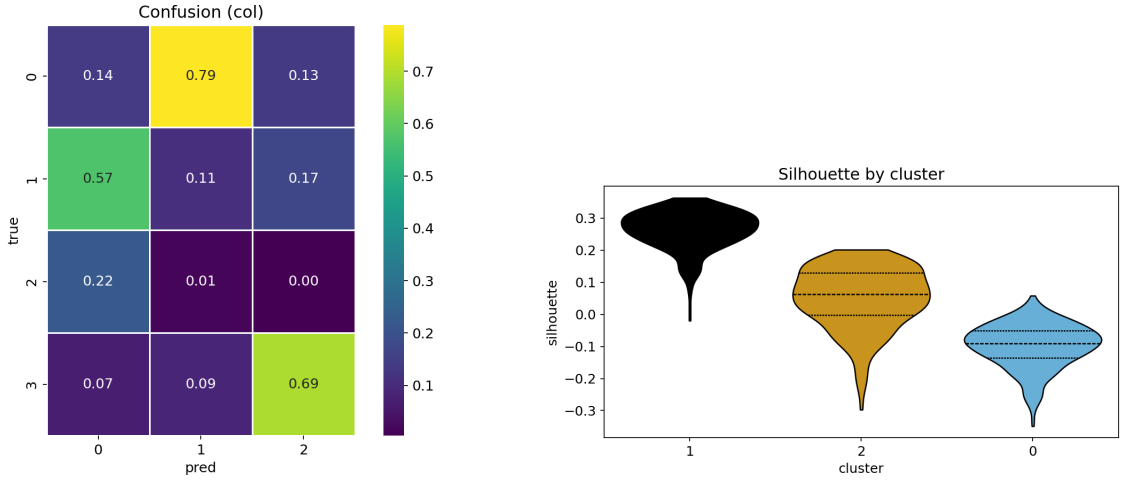


Figure 5: **Niche identification views (OSCC).** (a–c) illustrate Macro-Regions, Zonal Compartments, and Micro-Niches. (d) Consensus Structures derived from the final embeddings. (e) Reference annotations for comparison.



(a) Confusion matrix (column-normalized).

(b) Silhouette distributions per Consensus Structure.

Figure 6: **Clustering diagnostics (OSCC; final embeddings).** (a) Purity of predicted Consensus Structures relative to reference labels. (b) Cohesion/separation of each cluster in embedding space.

Results (OSCC). The segmentation-driven maps (Fig. 5) show how Macro-Regions, Zonal Compartments, and Micro-Niches provide complementary context. Predicted Consensus Structures broadly aligned with pathologist annotations, though some true niches were partially absorbed into broader clusters.

Embedding-based evaluation (Fig. 6) quantified these trends. One Consensus Structure mapped cleanly to a single true niche, while others captured mixtures—most notably, one true class lacked a dedicated cluster. Silhouette distributions echoed this: one cluster was compact and well separated ($s \approx 0.28$), a second moderately coherent ($s \approx 0.12$), and a third diffuse with near-zero or negative values.

Quantitatively, the final embedding achieved ARI = 0.357, NMI = 0.378, Homogeneity = 0.334, Completeness = 0.435, and V-measure = 0.378. Accuracy and purity were both ≈ 0.689 , with macro-F1 0.551 and weighted-F1 0.648. The global silhouette score was low (0.028), reflecting partial overlap between clusters. Together, these results show that anisotropy-aware CCC recovers major niche boundaries, especially at tumor–stroma interfaces, while highlighting residual noise that challenges perfect separability.

Biological contrast with BRCA. In BRCA, the short anisotropy coherence length ($L_c \approx 63$ px, $\sim 3h$) limited the ability of clustering to capture contiguous niches. Whereas OSCC Consensus Structures often followed tumor–stroma boundaries, BRCA embeddings produced more fragmented and overlapping groups, consistent with its heterogeneous stromal architecture. Thus, anisotropy-aware CCC improves niche identification where stromal coherence exists (OSCC), but has reduced leverage in more disorganized tissue (BRCA).

4.6 ECM/Collagen Case Study (S4.6)

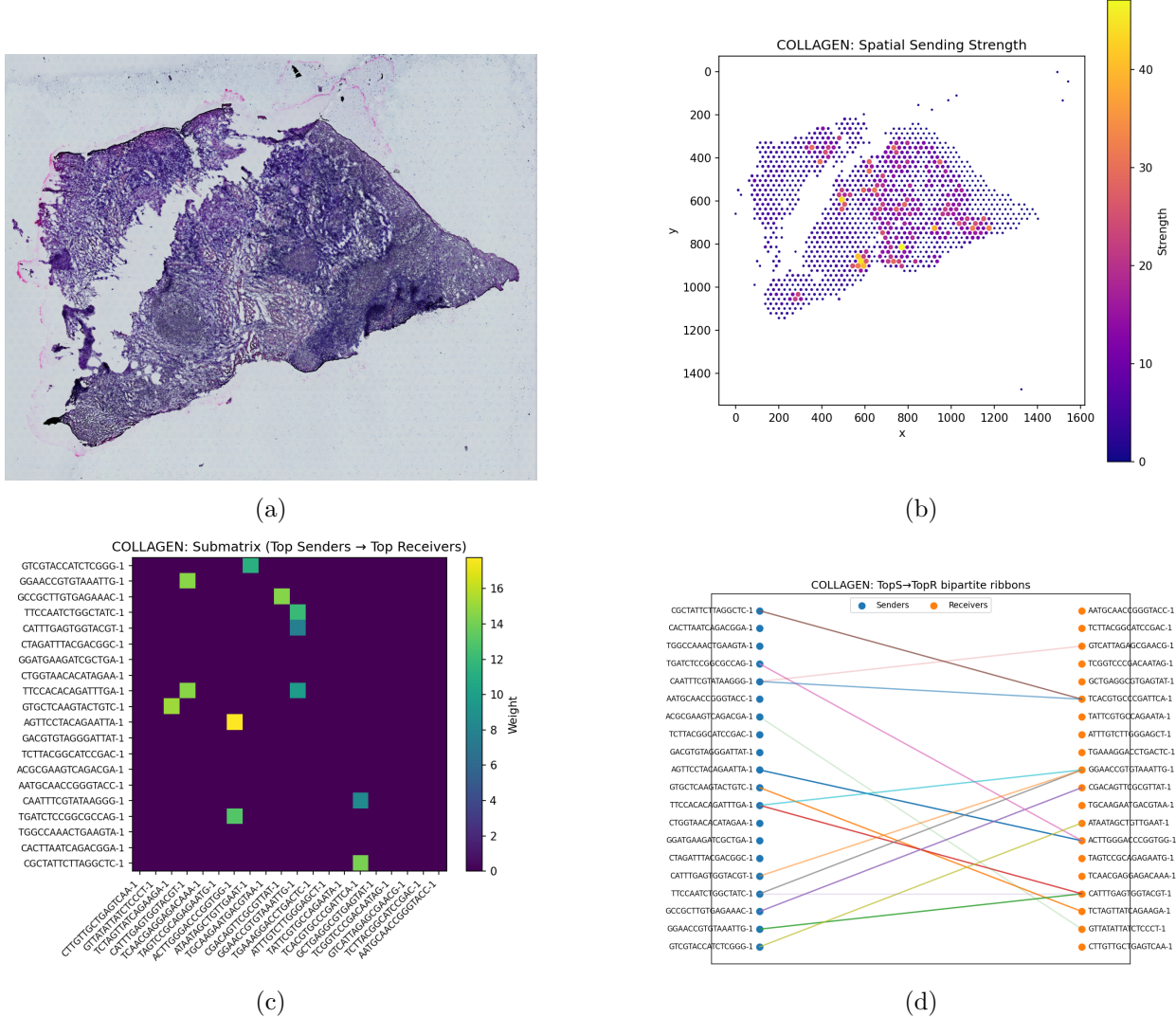
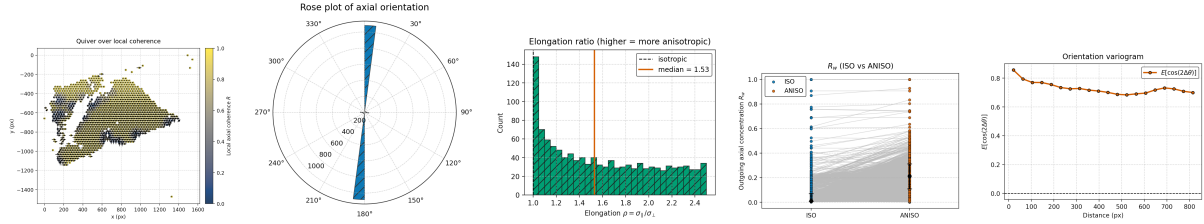


Figure 7: **ECM/Collagen pathway in OSCC (wv44).** (a) H&E tissue section. (b) Spatial sending strength highlights stromal regions adjacent to tumor epithelium. (c) Submatrix of the top-20 senders versus top-20 receivers reveals sparse but concentrated bundles of signaling. (d) Bipartite ribbons illustrate dominant stromal→epithelial communication flows.

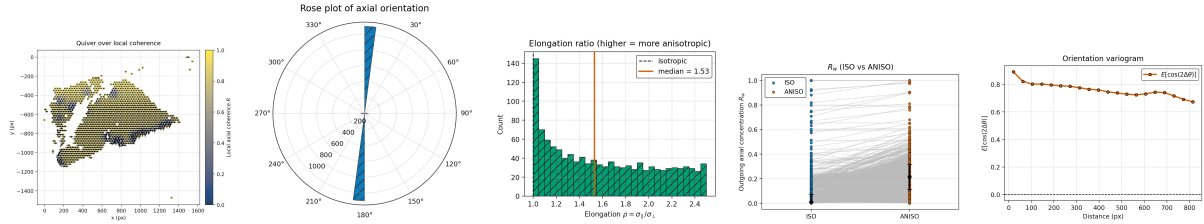
Supporting analyses are shown in Supplementary Fig. S14, including pathway correlation structure (panel a), Jaccard overlap of top senders (b), edge length–weight distributions (c), and cumulative mass contributions (d). Together, these results confirm that the ECM/Collagen pathway yields morphologically confined, anisotropy-aligned communication bundles at tumor–stroma interfaces.

4.7 Appendix: Cross-family Anisotropy Panels (S4.7)

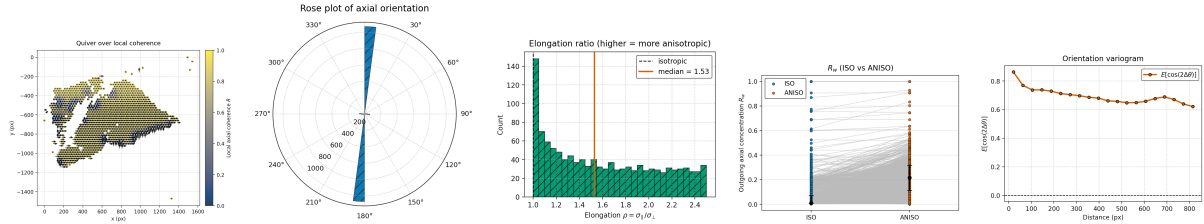
Panel key and notation. Each method shows: (a) quiver of dominant axis θ (arrow length \propto anisotropy, rescaled $a = (\rho - 1)/(\rho + 1)$); (b) rose of orientations with $\theta \equiv \theta + \pi$; (c) histogram of



wv22: (a) quiver; (b) rose; (c) elongation ρ ; (d) R_w ; (e) variogram.



wv23: (a) quiver; (b) rose; (c) elongation ρ ; (d) R_w ; (e) variogram.

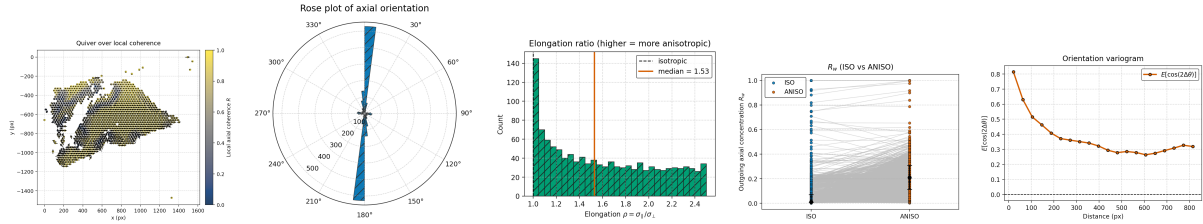


wv24: (a) quiver; (b) rose; (c) elongation ρ ; (d) R_w ; (e) variogram.

Suppl. Fig. S8 OSCC anisotropy panels for 2-band families (wv22/23/24).

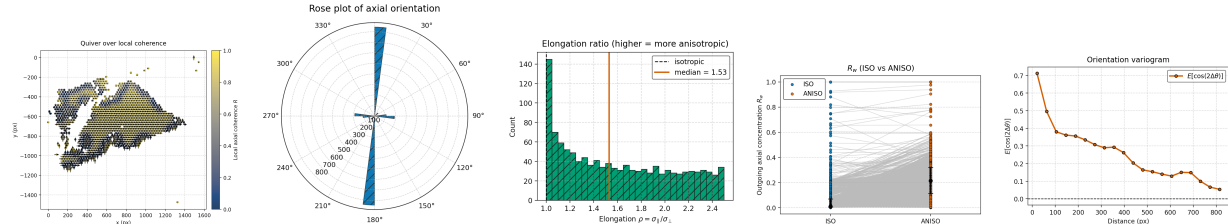
elongation $\rho = \sigma_{\parallel}/\sigma_{\perp}$; (d) outgoing angular concentration R_w (ISO vs. ANISO, area-matched); (e) orientation variogram with coherence length L_c at 0.2 crossing.

4.8 ECM/Collagen Support Figures (S4.8)

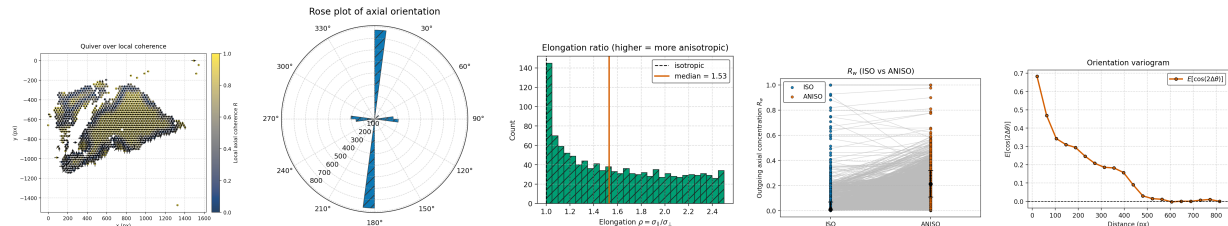


dtcwt: (a) quiver; (b) rose; (c) elongation ρ ; (d) R_w ; (e) variogram.

Suppl. Fig. S9 OSCC anisotropy panels for DTCWT ($N=1185$, median $h=25$ px).

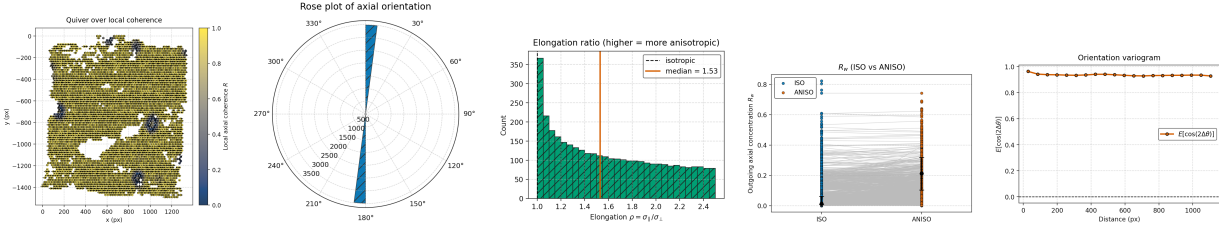


wv42: (a) quiver; (b) rose; (c) elongation ρ ; (d) R_w ; (e) variogram.

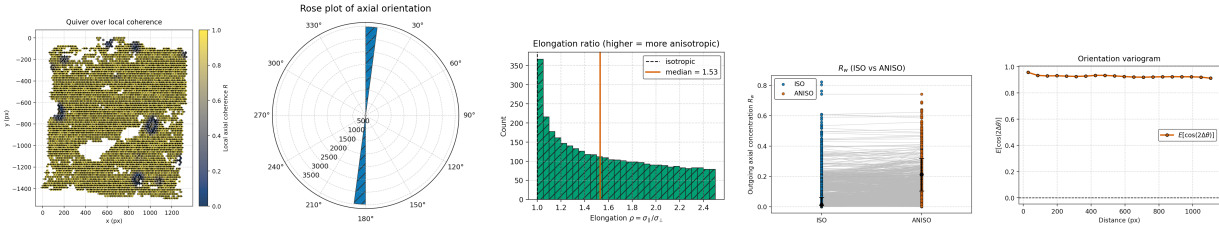


wv44: (a) quiver; (b) rose; (c) elongation ρ ; (d) R_w ; (e) variogram.

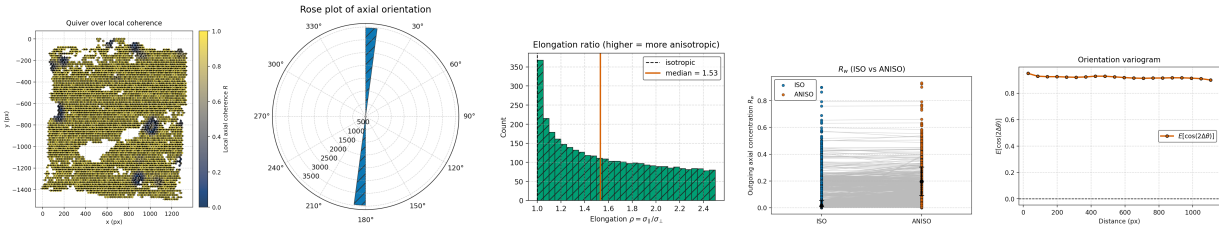
Suppl. Fig. S10 OSCC anisotropy panels for 4-band families (wv42/44).



wv22: (a) quiver; (b) rose; (c) elongation ρ ; (d) R_w ; (e) variogram.

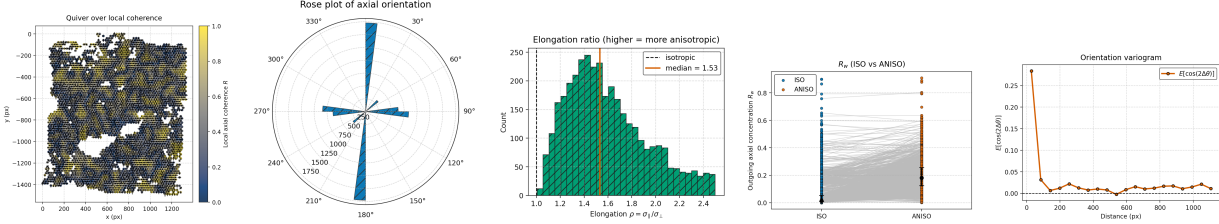


wv23: (a) quiver; (b) rose; (c) elongation ρ ; (d) R_w ; (e) variogram.

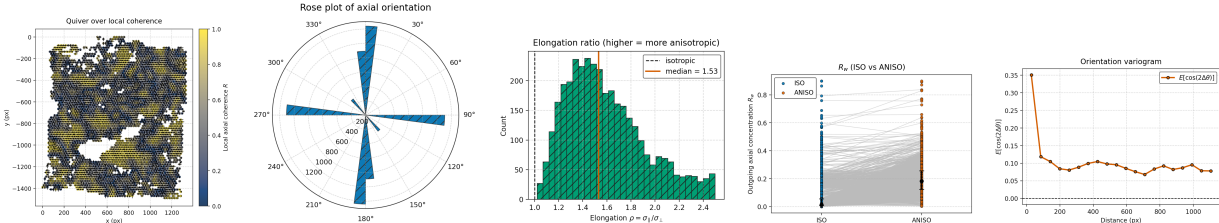


wv24: (a) quiver; (b) rose; (c) elongation ρ ; (d) R_w ; (e) variogram.

Suppl. Fig. S11 BRCA anisotropy panels for 2-band families (wv22/23/24; $N=3547$, median $h\approx 22$ px).

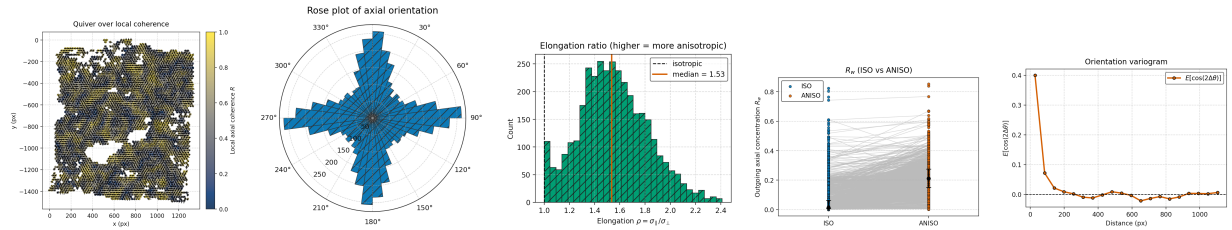


wv42: (a) quiver; (b) rose; (c) elongation ρ ; (d) R_w ; (e) variogram.



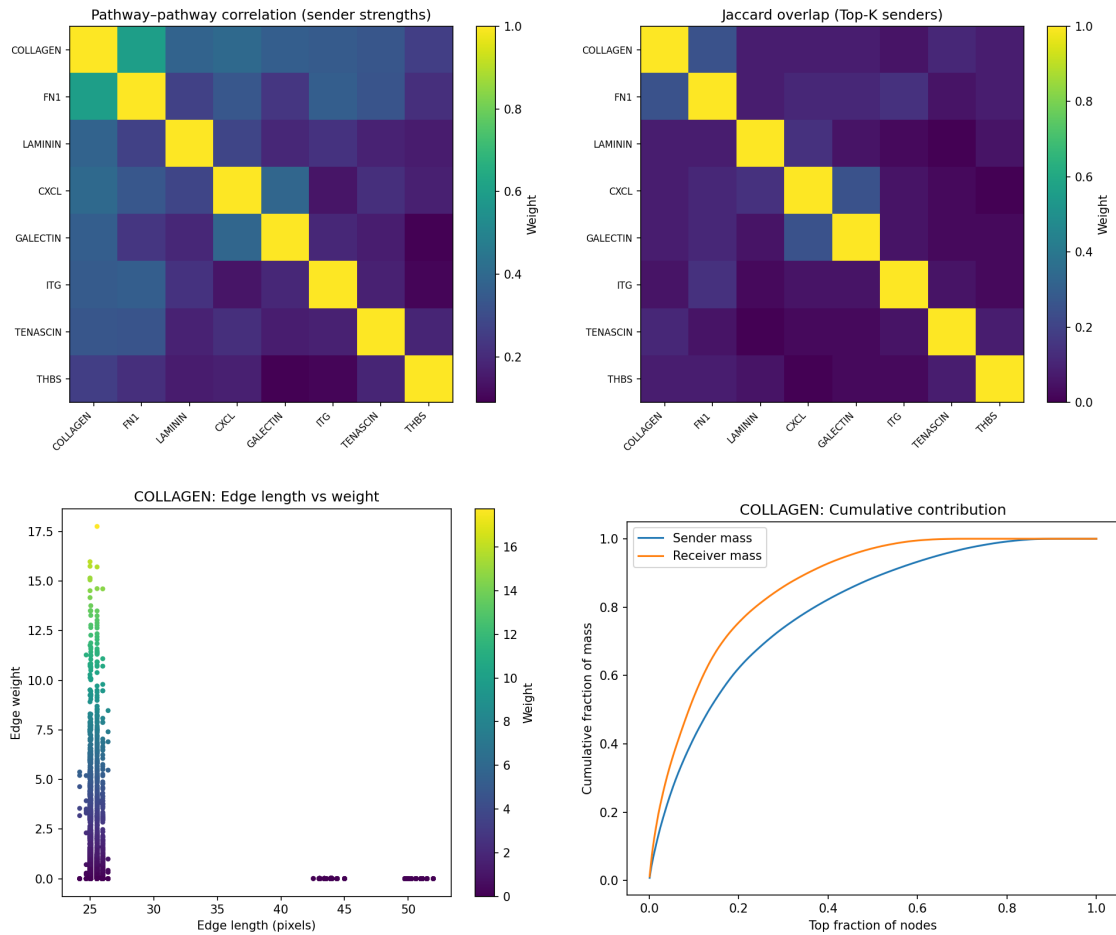
wv44: (a) quiver; (b) rose; (c) elongation ρ ; (d) R_w ; (e) variogram.

Suppl. Fig. S12 BRCA anisotropy panels for 4-band families (wv42/44).



dtcwt: (a) quiver; (b) rose; (c) elongation ρ ; (d) R_w ; (e) variogram.

Suppl. Fig. S13 BRCA anisotropy panels for DTCWT ($N=3547$, median $h \approx 22$ px).



Suppl. Fig. S14 OSCC (wv44) Collagen/ECM pathway support for the case study. (a) Pathway-pathway sender correlation heatmap. (b) Jaccard overlap of top- K senders ($K=20$). (c) Edge length vs. weight. (d) Cumulative contribution curves showing hub-like structure.